Published in final edited form as:
J Magn Reson Imaging. 2011 May ; 33(5): 1052–1062. doi:10.1002/jmri.22533.

Hyperpolarized Xenon-129 Gas-Exchange Imaging of Lung Microstructure: First Case Studies in Subjects with Obstructive Lung Disease

Isabel Dregely, MS[1], **John P. Mugler III, PhD**[2], **Iulian C. Ruset, PhD**[3], **Talissa A. Altes, MD**[2], **Jaime F. Mata, PhD**[2], **G. Wilson Miller, PhD**[2], **Jeffrey Ketel, BS**[3], **Steve Ketel, BS**[3], **Jan Distelbrink, PhD**[3], **F.W. Hersman, PhD**[1,3], and **Kai Ruppert, PhD**[2]

[1] Department of Physics, University of New Hampshire, Durham, NH

[2] Center for In-vivo Hyperpolarized Gas MR Imaging, Department of Radiology, University of Virginia School of Medicine, Charlottesville, VA

[3] Xemed LLC, Durham, NH

Abstract

Purpose—To develop and test a method to non-invasively assess the functional lung microstructure.

Materials and Methods—The Multiple exchange time Xenon polarization Transfer Contrast technique (MXTC) encodes xenon gas-exchange contrast at multiple delay times permitting two lung-function parameters to be derived: 1) MXTC-F, the long exchange-time depolarization value, which is proportional to the tissue to alveolar-volume ratio and 2) MXTC-S, the square root of the xenon exchange-time constant, which characterizes thickness and composition of alveolar septa. Three healthy volunteers, one asthmatic and two COPD (GOLD stage I and II) subjects were imaged with MXTC MRI. In a subset of subjects, hyperpolarized xenon-129 ADC MRI and CT imaging were also performed.

Results—The MXTC-S parameter was found to be elevated in subjects with lung disease (p-value = 0.018). In the MXTC-F parameter map it was feasible to identify regional loss of functional tissue in a COPD patient. Further, the MXTC-F map showed excellent regional correlation with CT and ADC ($\rho \geq 0.90$) in one COPD subject.

Conclusion—The functional tissue-density parameter MXTC-F showed regional agreement with other imaging techniques. The newly developed parameter MXTC-S, which characterizes the functional thickness of alveolar septa, has potential as a novel biomarker for regional parenchymal inflammation or thickening.

Keywords

hyperpolarized xenon-129; gas exchange; lung function

INTRODUCTION

Today, the clinical diagnosis for most lung diseases relies primarily on clinical history and global assessment of lung function provided by pulmonary function tests (PFTs). Imaging of

Address correspondence to: Isabel Dregely, University of New Hampshire, Physics Department, 9 Library Way, Durham, NH 03824, TEL: 603-988-5452, FAX: 603-862-2998, imu4@unh.edu.

lung structure using computed tomography (CT) is a useful adjunct for certain lung diseases. However, there currently exists no method for measuring regional gas exchange within the lung, and early diagnosis, phenotyping and monitoring of lung disease would greatly benefit from such a tool. The main physiological function of the lung is the exchange of respiratory gases from the alveolar air spaces, through the respiratory epithelium and capillary endothelium, into the blood. The size of relevant structures is on the micrometer scale (1), far below the resolution limit of current *in vivo* diagnostic imaging modalities.

The development of hyperpolarization methods for xenon-129 (2) led to its use as an inhaled contrast agent for MRI (3). Upon inhalation, hyperpolarized xenon-129 (HXe129) follows the functional pathway of gas exchange in the lung by diffusing from alveolar air spaces into alveolar septa, a structure 5–8 microns thick consisting of blood and tissue (1). HXe129 atoms dissolved in lung tissues exhibit a large chemical shift (~ 200 ppm) relative to their gas-phase resonance frequency (4), which enables image acquisition methods to distinguish gas- and dissolved-phase xenon (5–7), and permits imaging of lung function such as gas exchange (8–11) and alveolar-capillary gas uptake (12–14). Through modeling of xenon diffusion, physiologically important microstructure parameters, such as parenchymal tissue to alveolar-volume ratio (8–11), surface-to-volume ratio (11) and blood-gas barrier thickness (15), can be determined. However, the latter two have only been demonstrated in whole-lung spectroscopy experiments. The reasons for this are two-fold. First, due to the low partition coefficient (γ=0.1 (16)), the dissolved-phase xenon magnetization is much less than (~2%) the gas-phase magnetization. Second, in order to extract the wall thickness or surface-to-volume ratio, the xenon diffusion process has to be encoded at multiple time points. Imaging at multiple time points is fundamentally limited by SNR, since the magnetization of HXe129 is in a non-equilibrium state and is continuously depleted during image encoding. Furthermore, HXe129 acquisitions in humans are usually performed during breath-holding and multiple encodings proportionately lengthen the acquisition time.

The Xenon polarization Transfer Contrast (XTC) MR method pioneered by Ruppert and colleagues (8–10) overcomes the difficulty of imaging xenon in the dissolved phase by encoding xenon exchange information into the relatively large gas-phase signal. In this study, we implemented XTC MRI in four dimensions by extending the original single-exchange-time 2D-projection acquisition to a 3D acquisition that characterizes the gas-exchange process for multiple delay times. We call this method Multiple exchange time Xenon polarization Transfer Contrast, or MXTC.

By collecting data at multiple delay times, MXTC enables regional mapping of two lung-function parameters: 1) MXTC-F, the long exchange-time depolarization value, which is proportional to the ratio of functional tissue to alveolar volume and 2) MXTC-S, the square root of the xenon gas-exchange time constant, which is proportional to the ratio of septal wall thickness and the square root of xenon membrane diffusivity. Only structures in the lung parenchyma that are actively involved in the gas-exchange process contribute to image contrast. This makes the technique specifically sensitive to disease-induced alterations of lung microstructure that compromise gas exchange.

The goal of this study was to develop the MXTC technique and assess the potential utility of MXTC to detect disease-induced alterations of functional lung microstructure based on three case studies of obstructive lung disease. We describe preliminary findings of MXTC parameter mapping in three healthy subjects, two subjects with COPD and one subject with asthma. For the two COPD subjects, we also compared the results for MXTC-F, the functional tissue-density parameter, with HXe129 apparent diffusion coefficient (ADC) imaging, which probes alveolar size. Further, for one of the COPD subjects, we also

compared MXTC-F to CT imaging, the current gold standard to depict tissue destruction from emphysema.

BACKGROUND

A schematic of the MXTC pulse sequence is shown in Fig. 1. Conceptually, it is based on a single breath-hold implementation of XTC (for details, see ref. (8–11)). However, for the MXTC implementation, four 3D-FLASH image sets of gas-phase HXe129 are acquired (labeled I_1, I_2, I_3 and I_4), rather than three 2D-projection images as in ref. (11). These image sets are separated by a series of frequency-selective saturation pulses, centered either at −208 ppm relative to the gas phase for control contrast (applied between I_1 and I_2) or at +208 ppm to affect xenon-129 dissolved in blood and parenchymal tissue, and create XTC contrast (applied between I_2 and I_3 for the first XTC contrast of the image set, and between I_3 and I_4 for the second XTC contrast of the image set). After each saturation pulse during the XTC contrast-generation periods, the longitudinal magnetization in the dissolved phase is (ideally) destroyed. During the selected delay time τ between saturation pulses, HXe129 atoms in the gas phase exchange with xenon atoms in the dissolved phase, whose longitudinal magnetization is saturated. This results in a net decay of xenon magnetization in the gas phase. Repetition of this process results in a measurable reduction of gas-phase magnetization, creating XTC contrast. The control acquisition reflects all other contributions to the gas-phase signal decay (e.g., T1 and HXe129 removal by the blood stream) and is used for normalization purposes.

The sequence parameters for all four 3D acquisitions (I_i) are identical except for the excitation flip angle, which is increased for acquisitions I_3 and I_4 to maintain an adequate signal-to-noise ratio (SNR). In the following, only the analysis of the first XTC acquisition using I_2 and I_3 is described. The analysis based on I_3 and I_4 is performed in an analogous fashion. For acquisitions I_2 and I_3, the gas-phase depolarization per saturation pulse (f_τ) for a given delay time τ is calculated by normalizing the contrast ratio (I_3/I_2) with the control ratio (I_2/I_1) and accounting for the different excitation flip angles in the respective image acquisitions (α_1, α_2, α_3):

$$f_\tau = 1 - \left(\frac{I_3 I_1}{I_2^2} \cdot \frac{(\sin\alpha_2)^2 (\cos\alpha_1)^{N-K}}{\sin\alpha_3 \sin\alpha_1 (\cos\alpha_2)^{N-2K} (\cos\alpha_3)^K} \right)^{\frac{1}{N_p}}, \quad [1]$$

where I_i represents the signal intensities in the i^{th} FLASH image set, N_p is the total number of saturation pulses, N is the total number of image excitation pulses, and K is the number of image excitations before reaching the center of k-space.

While XTC MRI probes HXe129 exchange for only a single exchange time, MXTC MRI provides depolarization maps (f_τ) at several different delay times. The process of xenon exchange as a function of delay time can be modeled using the solution to the differential equation of Fick's second law of diffusion with Dirichlet boundary conditions. Thus, the magnetization loss in the gas phase due to xenon exchange after a 90° saturation RF pulse centered at the dissolved-phase region is given by (9):

$$f(\tau) = F\left(1 - \sum_{n=1}^{\infty} \frac{8}{((2n-1)\pi)^2} \exp\left(-D_m \left(\frac{(2n-1)\pi}{L_{\tilde{t}}}\right)^2 \tau\right)\right), \quad [2]$$

where F is the gas-phase depolarization for an infinitely long delay time and corresponds to the measurement parameter MXTC-F, D_m ($0.33*10^{-5}$ cm^2/s (9)) is the xenon diffusion constant in the septal wall, and L_t is the average functional septal wall thickness. At technically feasible delay times (> 5 ms), keeping only the first term in the infinite series is a good approximation:

$$f(\tau)=F\left(1-\frac{8}{\pi^2}\exp\left(-\frac{\tau}{\tau_c}\right)\right), \quad [3]$$

where τ_c is the exchange-time constant with which the saturated dissolved-phase magnetization is replenished:

$$\tau_c=\frac{L_t^2}{D_m\pi^2}. \quad [4]$$

Fitting of the measured gas-phase depolarization to Eq. [3] permits extraction of the maximum depolarization value MXTC-F and the exchange-time constant τ_c. At long delay times, all xenon atoms saturated in the dissolved phase exchange with the gas phase and thus the depolarization ratio (F) divided by the partition coefficient (Ostwald solubility γ=0.1 (16)) yields the tissue to alveolar-volume ratio:

$$\frac{V_t}{V_a}=\frac{F}{\lambda}. \quad [5]$$

V_t is the functional parenchymal tissue volume and V_a is the alveolar gas volume. Note that MXTC-derived parameters refer to the functional subset of structures in the lung parenchyma that are directly involved in gas exchange. We therefore use V_t, in order to distinguish it from the purely structural definition of parenchymal tissue volume V_t defined in the field of ex-vivo histology. Using the second fitting parameter, MXTC-S ($\mathrm{MXTC}-S=\sqrt{\tau_c}$), and Eq. [4], the average functional septal wall thickness L_t can be calculated as:

$$L_t=\sqrt{\tau_c D_m}\cdot\pi. \quad [6]$$

Note that by choosing a single, long exchange time for conventional XTC MRI, the parameter MXTC-F can be obtained using the previously reported single-exchange time XTC method. However, the MXTC implementation described in this paper is required to obtain MXTC-S, the wall-thickness parameter derived from the HXe129 dynamic exchange process.

Since, in this study, MXTC was implemented with a non-selective saturation of the dissolved-phase magnetization, no distinction is made between red blood cell and tissue compartments within the parenchyma. Therefore the functional wall thickness L_t refers to the entire septal wall.

MATERIALS AND METHODS

General Study Protocol

For this preliminary study, three healthy, non-smoking volunteers, two subjects with COPD and one with asthma (Table 1) were recruited. Before each imaging procedure, written informed consent was obtained from the subject after the nature of the procedure had been fully explained. Spirometry was performed immediately before and after the imaging session (Table 1). Before the subject was placed in the RF coil, a test dose of xenon was administered. All subjects tolerated the test dose well although some had mild central nervous system effects such as mild transient numbness or tingling, and alterations in affect.

For HXe129 imaging studies, subjects breathed in the HXe129 dose (500 ml) simultaneously with an oxygen-air mixture (135 ml oxygen, 100 ml air) starting from RV. Therefore the absolute lung volume for imaging studies can be roughly estimated to be slightly below FRC. MXTC studies were performed on a whole-body 3T MRI system (TIM Trio, Siemens Medical Solutions, Malvern, PA) and used a custom-built 32-channel receive array with integrated asymmetric birdcage transmit coil (17). ADC studies were performed on a 1.5T MRI system (Avanto, Siemens Medical Solutions, Malvern, PA) using a flexible transmit/receive chest RF coil (IGC Medical Advances, Milwaukee, WI). During imaging, blood oxygenation was monitored. A physician supervised each MRI examination.

Hyperpolarized-Gas Production

Xenon-129 was polarized using a commercial prototype system (Xemed LLC, Durham, NH) (18) via spin-exchange optical pumping (2,18,19). For each set of experiments, two liters of xenon gas were accumulated in the frozen state. Subsequently, the gas was thawed into four 500-ml Tedlar bags for four breath-hold imaging experiments. In order to maintain at least 21% oxygen entering the lungs, each HXe129 dose was administered together with an oxygen-air mixture as described above.

Imaging Protocols

The MXTC pulse sequence as outlined in Fig. 1 and described in the Background section was implemented on our 3T MR scanner. Flip angles were calibrated based on results from previous B1 mapping of the custom-built 32-channel array RF coil, as described in reference 20, which found that the standard deviation of the flip-angle values within the lung was only 8% of the mean flip-angle value. Analogous measurements performed in other human subjects (unpublished data) found similarly small variations in flip-angle values within the lung. These previous results also indicated that variations in coil loading due to body habitus have negligible effect on transmitter calibration values, possibly due to the large size of the transmitter coil and the presence of the receiver coil array. Therefore, B1 maps were not measured for each subject in this study, and the flip angle was approximated as being constant across the lung volume.

The gas-phase FLASH acquisitions in the MXTC pulse sequence used conventional Cartesian *k*-space sampling with sequential phase-encoding and a constant flip angle. The imaging parameters for the FLASH acquisitions were: TR/TE 7.7/2.5 ms, image resolution $9.2 \times 9.2 \times 21–24$ mm^3, matrix $48 \times 30 \times 10$, acceleration factor 3, reference lines 21, and receiver bandwidth 260 Hz/pixel. Non-selective, 500-μs, rectangular RF pulses with flip angles of 1°, 1°, 2° and 4° were used for acquisitions I_1, I_2, I_3 and I_4, respectively. The flip angles for I_3 and I_4 were higher to maintain adequate SNR.

Imaging and contrast parameters for MXTC were adjusted for each patient considering factors such as lung size (affecting spatial resolution and image matrix) and disease state,

while maintaining a total acquisition time of no more than 20 s. For example, in COPD with emphysematous tissue loss, the number of contrast-generating RF pulses was increased to maintain a total gas-phase depolarization of ~40%. The 20-s acquisition time constraint was not a limitation for short delay times, but sometimes required the number of contrast-generating RF pulses for long delay times to be reduced below the ideal value. The total acquisition time is given by:

$$TA_{total}=4\times TA(I)+N_1\cdot\tau_1\cdot 2+N_2\cdot\tau_2. \quad [7]$$

Here, TA_{total} is the total acquisition time (ranging from 10–20 s), $TA(I)$ is the acquisition time for each gas-phase 3D-FLASH acquisition (1.5–2.2 s, depending on subject lung size), N_1 (N_2) is the number of contrast-generating RF pulses and τ_1 (τ_2) is the delay time between these RF pulses during the control and first (second) XTC contrast-generation steps. The settings for N and τ are summarized in Table 2.

At least two breath-holds were performed in each subject to obtain the four delay-time points (two delay-time contrasts per breath-hold) required for the two-parameter fit for MXTC-F and MXTC-S. The delay-time points were chosen to cover the expected range of the exponential curve; the shortest, technically feasible delay time (5 ms) was always used and the maximum delay time for a given subject was at least 40 ms. If circumstances allowed (i.e., willingness of subject, availability of sufficient polarized xenon, etc.), additional breath-holds were performed, and included three in subjects H2 and C1, and four in subjects H1 and C2 (Table 2). To minimize registration errors due to different breath-hold positions, identical xenon doses and breath-hold maneuvers were used for each acquisition.

Contrast-generating RF pulses were 3-ms Gaussian pulses with a flip angle of 75°, rather than the ideal value of 90°. Due to hardware limitations on the 3T scanner, the flip angle for the saturation RF pulses was limited to a maximum of 75°, resulting in incomplete saturation of xenon magnetization in the dissolved phase (21). Therefore, the XTC maps obtained underestimated depolarization. A correction factor for the computation of XTC contrast maps was determined from spectroscopic XTC experiments performed at 1.5T by comparing the gas-phase depolarization for 75° saturation pulses to that for 90° pulses. (This correction factor will be confirmed by additional studies in the future; while it affects the quantitative values in MXTC maps it does not change their qualitative appearance. Further, knowledge of the precise factor is not required to perform comparison of maps acquired in different subjects but using identical experimental parameters.)

Apparent diffusion coefficient (ADC) imaging in humans has been studied extensively with hyperpolarized He-3 (22–25) and successfully applied to probe alveolar size (26). However, there is much less experience with ADC imaging in humans using HXe129. In this study, HXe129 short-time scale ADC maps were acquired using a standard interleaved, two *b*-value (0 and 10 s/cm^2), slice-selective 2D-GRE implementation with a diffusion time of 3.2 ms. Other imaging parameters were: TR/TE 14/10 ms, flip angle 7.5°, image resolution 5 × 5 × 30 mm^3, matrix 96 × 66, slices 6, and receiver bandwidth 220 Hz/pixel.

CT data were obtained from a GE Light Speed 16 detector-row CT scanner (GE Medical Systems, Milwaukee, WI). Each scan was acquired during a short breath-hold after the patient was told to take a deep breath and hold it. Coronal image slices were reconstructed at 5-mm slice thickness for the identification of emphysematous regions and additionally at 20-mm slice thickness for comparison to hyperpolarized-gas imaging techniques.

Data Analysis

MXTC data were analyzed offline using MATLAB (Mathworks, Natick, MA). Accelerated image acquisitions were reconstructed using the GRAPPA algorithm (27). Background noise was masked from the images and depolarization maps f_τ for each delay time τ were generated from the corresponding FLASH image sets using Eq 1. As discussed earlier, resulting depolarization maps were multiplied by a correction factor, which was found to be 1.5, to compensate for using 75° instead of 90° contrast-generating RF pulses. A complete MXTC data set consisted of at least four XTC maps obtained at different characteristic exchange times τ.

MXTC parameter maps were generated on a voxel-by-voxel basis using non-linear least-squares fitting of the depolarization data as a function of τ to Eq. [3]. The fitting quality was assessed using the distribution of the reduced χ^2-statistics ($Q(\chi^2/\upsilon, \upsilon)$, where υ is the number of degrees of freedom). For the calculation of χ^2, the standard deviation of f-values (Eq. [1]) within a given image slice was used as an estimate for the measurement error. Since this approach includes variability due to tissue heterogeneity as well, the result provides an upper bound for the error estimate. Poor voxel fits with a large χ^2 ($Q < 0.05$) were rejected and the voxel fit parameters were marked as invalid and excluded from further analysis.

ADC maps were calculated using the noise-masked image ratio ($I_{ADC,2}$ / $I_{ADC,1}$) and *b*-value (10 s/cm^2):

$$ADC = -\frac{1}{b}\ln\left(\frac{I_{ADC,2}}{I_{ADC,1}}\right), \quad [8]$$

where $I_{ADC,1}$ and $I_{ADC,2}$ are the signal intensities in the b=0 and b=10 s/cm^2 images, respectively.

For COPD subject C2, CT data were reconstructed coronally for comparison with the coronal MR acquisitions. Regions of emphysema were defined as pixels in the lung with attenuation less than −950 HU (28).

Statistical Analysis

To illustrate gravity-induced deformation of lung tissue, linear fitting of the median for each coronal image as a function of lung "height" (i.e., distance along the anterior-posterior direction, measured from the most posterior image) was performed. Significance was evaluated using Student's *t*-test comparing the calculated anterior-posterior slope to zero. Differences between the three healthy subjects (H1, H2, and H3) and the three subjects with obstructive lung disease (C1, C2, and A1) were evaluated using Student's *t*-test, comparing healthy and disease group means, where a group consisted of the three individual subjects' whole-lung medians for MXTC-F and MXTC-S, respectively. In order to quantify the extent of agreement between different imaging modalities, each image was segmented into eight regions of interest (ROIs) and the correlation of values corresponding to the ROIs from different imaging modalities was determined. The strength of correlation was quantified using Spearman's rank correlation coefficient ρ.

RESULTS

MXTC Parameters In Subjects With Lung Disease Compared To Healthy Volunteers

Maps of the two MXTC parameters from healthy volunteers (subjects H1–H3) were generally homogeneous within each coronal image slice, but increased values were observed

towards the posterior of the lung (Fig. 2a, b). This observation is consistent with the effect of gravity-induced lung-tissue compression in dependent lung regions (29–33), which are the posterior image slices for a subject in supine position. The MXTC parameter maps from the two COPD subjects C1 (GOLD stage I, FEV_1/FVC = 0.66, FEV_1 = 81% predicted) and C2 (GOLD stage II, FEV_1/FVC = 0.66, FEV_1 = 71% predicted) appeared to be considerably more heterogeneous (Fig. 2c, d [subject C1] and e, f [subject C2]). Further, the parameter maps for the COPD subjects differed from those of the healthy subjects and also from each other. For the asthmatic subject (subject A1), the maps for the tissue density parameter MXTC-F appeared similar to those for healthy volunteers. The group mean of three disease subjects' whole-lung medians for the septal-thickness parameter MXTC-S was significantly elevated (p-value = 0.018) compared to the group mean of three healthy subjects' whole-lung medians. For MXTC-F no significant whole-lung differences between the healthy and diseased groups were found (p-value = 0.35). However, as discussed below, for one of the subjects with lung disease, the regional differences were substantial.

To analyze differences among the parameter maps in more detail, we quantified the anterior-posterior (AP) parameter dependence by plotting the median MXTC parameter values for each image slice as a function of lung height (Fig. 3). Linear fitting showed that all healthy volunteers had a statistically significant ($p<0.05$) negative AP-gradient slope for the MXTC-F parameter. A negative slope corresponds to increased parameter values in posterior images, consistent with the gravitational tissue-compression effect. In contrast, COPD subject C1 did not exhibit a significant AP-slope for the MXTC-F parameter (Fig. 2c, Fig. 3a and Table 1), while COPD subject C2 had increased MXTC-F parameter values in posterior images. However, the AP dependence for subject C2 was not statistically significant (Fig. 2e, 3a and Table 1). This subject also had regions of decreased MXTC-F (Fig. 2e) within images, resulting in overall lower median values for anterior images compared to the parameter range in healthy subjects (Fig. 3a). The results for the asthmatic subject A1 (FEV_1/FVC = 0.64, FEV_1 = 74% predicted) was similar to the results of the normal volunteers for the MXTC-F parameter with a significant, negative slope along the AP direction (Fig. 3a and Table 1).

The AP-slope for the wall-thickness parameter MXTC-S was statistically significant and negative for all three healthy volunteers (H1-H3), but the relative changes were less than those associated with the AP-slope for MXTC-F (Fig. 3, Table 1). For subjects C2 and A1, the slope of the wall-thickness parameter MXTC-S along the AP direction was not significant, whereas for subject C1 the slope was found to be positive, corresponding to increased parameter values in the non-dependent anterior images (Fig. 3b, Table 1). For the subjects with lung disease, the medians of the MXTC-S parameter were elevated either in all coronal images (subject C2), or in all but the most posterior images (subjects C1 and A1), relative to those observed for the three healthy volunteers (Fig. 3b).

MXTC-F Compared To Other Imaging Techniques

The CT data for subject C2 demonstrated a statistically significant and positive dependence on lung height, in concordance with MXTC-F results in this subject. The AP dependence of ADC measurements was not statistically significant in any of the three subjects in whom ADC imaging was performed (H3, C1, C2, Table 1).

From the CT data for subject C2, we identified regions of emphysema by applying a threshold of −950 HU. These data were treated as the "gold standard" to locate regions of emphysema (28) in this particular subject and compared to results from the HXe129 imaging techniques. Parameter maps for MXTC-F and ADC appeared qualitatively similar to the CT data, with regions of abnormally low (MXTC-F) or high (ADC) parameter values identifying emphysematous tissue destruction in the upper lobes of this subject (white

arrows in Fig. 4). Regional comparisons among MXTC-F, ADC and CT in COPD subject C2 resulted in high correlations (Spearman's $\rho = 0.88–0.94$) (Fig. 5). For COPD subject C1 and for healthy subject H3, regional comparison among MXTC-F and ADC resulted in lower correlations ($\rho = 0.56$ and $\rho = 0.11$, respectively), most likely because the parameter distribution in subject C1 was fairly homogeneous throughout the lung and did not show distinct regional differences, and for subject H3, ADC, unlike MXTC-F, did not show a statistically significant AP dependence.

Histograms in Fig. 6 reveal distinct differences in the parameter distributions of "healthy" and "emphysematous" regions in subject C2.

DISCUSSION

In this preliminary study we have shown that MXTC has the potential to provide a regional assessment of gas exchange and yields two parameters linked to physiologically important characteristic of the lung microstructure: 1) MXTC-F, which is proportional to the ratio of functional lung tissue to alveolar volume, and 2) MXTC-S, which is proportional to the functional septal wall thickness and also reflects xenon diffusivity in the septa. Acquiring both parameters simultaneously allows a change in relative tissue density (MXTC-F), induced by a change in the number of alveolar walls per unit volume (e.g., emphysematous tissue destruction resulting in enlarged air spaces), to be discriminated from a change in the alveolar wall thickness (MXTC-S). The main findings of this study were the excellent regional correlation of MXTC-F with HXe129 ADC MRI and with CT in one subject, and the observation of increased MXTC-S in subjects with lung disease, potentially indicating parenchymal thickening possibly due to inflammation.

Emphysematous lung is defined as an "[…] abnormal, permanent enlargement of air spaces distal to the terminal bronchiole, accompanied by the destruction of their walls […]" (34). These pathological changes in lung microstructure were assessed in COPD subject 2 (GOLD stage II) by two imaging modalities that are sensitive to tissue density (MXTC-Fand CT) and one that reflects airspace size (HXe129 ADC). For the emphysematous regions identified in this subject, we found excellent regional correlation between the experimental HXe129 imaging techniques and the clinically established imaging modality CT. However, since MXTC-F is based on xenon gas exchange in the lung parenchyma, this parameter represents true functional information, whereas both CT and ADC imaging represent structure, which only indirectly leads to lung function information via the structure-function relationship. Unlike COPD subject C2, subject C1 (GOLD stage I) exhibited no distinct regions in the MXTC-F maps that were consistent with the expected appearance of emphysema. On the other hand, this subject appeared distinctly different from healthy volunteers due to the absence of a gravity-induced AP-gradient in median MXTC-F values.

The potential functional importance of MXTC-S is evident, given that an increase in alveolar wall thickness is a known factor in compromising the efficiency of gas exchange. In this preliminary study, the MXTC-S parameter whole-lung medians in three subjects with obstructive lung disease were found to be significantly elevated compared to those in three healthy subjects. Even though the three subjects were characterized by different phenotypes of obstructive disease, which led to distinctly different MXTC-F maps (normal appearance for asthma, regional emphysema in COPD GOLD stage II, no AP-gradient in COPD GOLD stage I), their MXTC-S parameters were qualitatively consistent, being statistically significantly elevated compared to the three healthy subjects. Since we believe that increased MXTC-S indicates septal wall thickening, our results suggest the possibility of parenchymal inflammation, which is known to be a consistent finding in COPD and asthma (35). A study by Vlahovic and colleagues (36) found a significant correlation between the

degree of emphysema and the thickening of alveolar walls, which would support our hypothesis that increased MXTC-S is related to septal wall thickening. However, the same study also revealed an increase in the amounts of elastin and collagen relative to other constituents in the membranes. Since MXTC-S is related to wall thickness and the xenon diffusivity, this raises the question as to whether an observed increase in MXTC-S is due to an increase in membrane thickness or due to a change in xenon diffusivity caused by compositional change of the septal walls, or a combination of both. An increase in membrane thickness could be accompanied by decreased lung compliance impeding gravitational lung tissue deformation, which could be a possible explanation for the absence of gravitational AP-gradients in our MXTC-S results in subjects with lung disease. Studies in a larger subject population, as well as in animal models with accompanying histology, are required to further investigate the relationship between the MXTC-S parameter and lung microstructure. However, it is already apparent from this study that the regional mapping of MXTC-S has the potential to become a powerful biomarker to non-invasively monitor disease progression and/or response to treatment by characterizing parenchymal inflammation and/or lung remodeling. To our knowledge, no other means of non-invasively estimating regional septal wall thickness or composition exist.

The practical application of MXTC was facilitated by increased HXe129 polarization levels (18,19), as well as by advances in RF coil technology (17). A custom-made, phased-array, human-chest receiver RF coil permitted a reduction in acquisition time by parallel imaging, which allowed us to encode two delay-time points in a single breath-hold. An integrated birdcage transmit coil provided good B1-excitation homogeneity, which was crucial for unbiased contrast generation. However, a trade-off in this integrated coil design was found in the relatively low transmit-power efficiency. Together with the constraint of the maximum available power from the RF power amplifier (6.5 kW at the xenon-129 frequency [broadband amplifier] compared to 35 kW for proton applications using the body coil [narrowband amplifier]), this resulted in a limitation in the current implementation of MXTC that, due to insufficient transmit-B1 amplitude, a maximum flip angle of 75° could be applied for the 3-ms Gaussian contrast-generating RF pulses. However, in order to completely saturate the dissolved phase, shorter-duration 90° flip angles are ideally required. Our attempt to correct for this effect, by comparing 75° and 90° spectroscopy-based XTC results and deriving a constant correction factor, is prone to error. Therefore, we did not attempt to derive absolute results for tissue to alveolar-volume ratio and wall thickness from the MXTC parameters in this study. We further note that the uncertainty in the correction factor does not affect the main findings of this preliminary study, since data for all subjects were obtained and analyzed in the same way, and the main findings are a relative increase of the time constant for diseased subjects compared to that for healthy subjects, and the regional correlation among different imaging techniques. In future studies, absolute determination of the tissue to alveolar-volume ratio and wall thickness can be achieved by addressing the flip-angle limitation. There are several possibilities based on either a hardware solution, e.g. by implementing a more powerful broadband RF amplifier for hyperpolarized-gas studies, or on a software solution, e.g. by focusing on selective MXTC, which selectively encodes xenon gas exchange for tissue and blood resonances, as described in (37). The higher spectral selectivity requires longer RF pulses, which will allow a 90° flip angle to be achieved with our current hardware.

In the current implementation, MXTC is a multi-breath experiment. It is therefore prone to spatial-registration errors secondary to different breath-hold positions. This issue can be addressed in future studies by implementing image-registration algorithms in the data analysis workflow (38). It is also possible that only two XTC contrasts at two different delay times may be sufficient to derive a difference parameter, instead of the xenon exchange-time constant parameter S, having equivalent diagnostic value for characterizing disease-induced

changes in the alveolar wall. This would make MXTC a single breath-hold technique, which not only has the benefit of eliminating spatial-registration errors, but is also important for clinical application.

In conclusion, this work demonstrates the first *in vivo* simultaneous mapping of lung microstructure parameters related to the tissue to alveolar-volume ratio and septal wall thickness in human subjects. Our preliminary results have shown that functional tissue-volume mapping with MXTC-F exhibits excellent correlation with HXe129 ADC MRI and with lung-tissue attenuation assessed by CT in one COPD patient with emphysematous tissue destruction. Furthermore, we demonstrated that the new microstructure parameter MXTC-S, which is proportional to the functional septal wall thickness, was elevated in subjects with lung disease. We therefore propose that MXTC-S could become a novel biomarker to characterize parenchymal inflammation or thickening with clinical applications to non-invasively monitor disease progression or treatment response. By quantifying two functional lung parameters, MXTC provides a more comprehensive picture of lung microstructure than existing imaging techniques, and could become an important non-invasive and quantitative tool to characterize pulmonary disease phenotypes.

Acknowledgments

Grant Support: NIH grants R42 HL082013 and R01 HL079077, and Siemens Medical Solutions

References

1. Weibel ER. What makes a good lung? Swiss Med Weekly. 2009; 139(27–28):375–86.
2. Happer W, Miron E, Schaefer S, Schreiber D, van Wijngaarden WA, Zeng X. Polarization of the nuclear spins of noble-gas atoms by spin exchange with optically pumped alkali-metal atoms. Phys Rev A. 1984; 29(6):3092–3110.
3. Albert MS, Cates GD, Driehuys B, et al. Biological magnetic resonance imaging using laser-polarized 129Xe. Nature. 1994; 370(6486):199–201. [PubMed: 8028666]
4. Miller KW, Reo NV, Uiterkamp AJS, Stengle DP, Stengle TR, Williamson KL. Xenon NMR: chemical shifts of a general anesthetic in common solvents, proteins, and membranes. Proc Natl Acad Sci USA. 1981; 78(8):4946–4949. [PubMed: 6946442]
5. Wagshul ME, Button TM, Li HF, et al. In vivo MR imaging and spectroscopy using hyperpolarized 129Xe. Magn Reson Med. 1996; 36(2):183–191. [PubMed: 8843370]
6. Mugler JP 3rd, Driehuys B, Brookeman JR, et al. MR imaging and spectroscopy using hyperpolarized 129Xe gas: preliminary human results. Magn Reson Med. 1997; 37(6):809–815. [PubMed: 9178229]
7. Swanson SD, Rosen MS, Coulter KP, Welsh RC, Chupp TE. Distribution and dynamics of laser-polarized (129)Xe magnetization in vivo. Magn Reson Med. 1999; 42(6):1137–45. [PubMed: 10571936]
8. Ruppert K, Brookeman J, Hagspiel K, Mugler JP 3rd. Probing lung physiology with xenon polarization transfer contrast (XTC). Magn Reson Med. 2000; 44(3):349–357. [PubMed: 10975884]
9. Ruppert K, Mata JF, Brookeman JR, Hagspiel KD, Mugler JP 3rd. Exploring lung function with hyperpolarized (129)Xe nuclear magnetic resonance. Magn Reson Med. 2004; 51(4):676–687. [PubMed: 15065239]
10. Ruppert K, Mata JF, Wang H-TJ, Tobias WA, Cates GD, Brookeman JR, Hagspiel KD, Mugler JP 3rd. XTC MRI: sensitivity improvement through parameter optimization. Magn Reson Med. 2007; 57(6):1099–1109. [PubMed: 17534927]
11. Patz S, Muradian I, Hrovat MI, et al. Human pulmonary imaging and spectroscopy with hyperpolarized 129Xe at 0.2T. Acad Radiol. 2008; 15(6):713–727. [PubMed: 18486008]
12. Driehuys B, Cofer GP, Pollaro J, Mackel JB, Hedlund LW, Johnson GA. Imaging alveolar-capillary gas transfer using hyperpolarized 129Xe MRI. Proc Natl Acad Sci U S A. 2006; 103(48): 18278–18283. [PubMed: 17101964]

13. Mugler JP 3rd, Altes TA, Ruset IC, et al. Simultaneous magnetic resonance imaging of ventilation distribution and gas uptake in the human lung using hyperpolarized xenon-129. Proc Natl Acad Sci U S A. 2010 PNAS published ahead of print November 22, 2010. 10.1073/pnas.1011912107
14. Cleveland ZI, Cofer GP, Metz G, et al. Hyperpolarized 129Xe MR Imaging of alveolar gas uptake in humans. PLoS ONE. 2010; 5(8):e12192. [PubMed: 20808950]
15. Mansson S, Wolber J, Driehuys B, Wollmer P, Golman K. Characterization of diffusing capacity and perfusion of the rat lung in a lipopolysaccaride disease model using hyperpolarized 129Xe. Magn Reson Med. 2003; 50(6):1170–1179. [PubMed: 14648564]
16. Goto T, Suwa K, Uezono S, Ichinose F, Uchiyama M, Morita S. The blood-gas partition coefficient of xenon may be lower than generally accepted. Br J Anaesth. 1998; 80(2):255–256. [PubMed: 9602599]
17. Dregely, IM.; Wiggins, GC.; Ruset, IC., et al. A 32 channel phased array lung coil for parallel imaging with hyperpolarized xenon 129 at 3T. Proceedings of the 17th Scientific Meeting of ISMRM; Honolulu. 2009. (abstract 4918)
18. Hersman FW, Ruset IC, Ketel S, et al. Large production system for hyperpolarized 129Xe for human lung imaging studies. Acad Radiol. 2008; 15(6):683–692. [PubMed: 18486005]
19. Ruset IC, Ketel S, Hersman FW. Optical pumping system design for large production of hyperpolarized. Phys Rev Lett. 2006; 96(5):053002. [PubMed: 16486926]
20. Dabaghyan, M.; Dregely, I.; Muradyan, I.; Hrovat, I.; Hatabu, H.; Butler, JP.; Patz, S. Oxygen partial pressure and uptake in the lung with hyperpolarized 129Xe MRI: Preliminary Results. Proceedings of the 18th Scientific Meeting of ISMRM; Stockholm. 2010. (abstract 987)
21. Hrovat, M.; Muradian, I.; Frederick, E.; Butler, J.; Hatabu, H.; Patz, S. Theoretical model for XTC (Xenon Transfer Contrast) experiments with hyperpolarized 129Xe. Proceedings of the 18th Scientific Meeting of ISMRM; Stockholm. 2010. (abstract 2556)
22. Salerno M, de Lange EE, Altes TA, Truwit JD, Brookeman JR, Mugler JP 3rd. Emphysema: hyperpolarized helium 3 diffusion MR imaging of the lungs compared with spirometric indexes–initial experience. Radiology. 2002; 222(1):252–260. [PubMed: 11756734]
23. Fain SB, Panth SR, Evans MD, et al. Early emphysematous changes in asymptomatic smokers: detection with 3He MR imaging. Radiology. 2006; 239(3):875–883. [PubMed: 16714465]
24. O'Halloran RL, Holmes JH, Altes TA, Salerno M, Fain SB. The effects of SNR on ADC measurements in diffusion-weighted hyperpolarized He-3 MRI. J Magn Reson. 2007; 185(1):42–49. [PubMed: 17150391]
25. van Beek EJR, Dahmen M, Stavngaard T, et al. Hyperpolarised 3He MRI versus HRCT in COPD and normal volunteers: PHIL trial. ERJ. 2009; 34(6):1311–21.
26. Yablonskiy DA, Sukstanskii AL, Leawoods JC, et al. Quantitative in vivo assessment of lung microstructure at the alveolar level with hyperpolarized 3He diffusion MRI. Proc Natl Acad Sci USA. 2002; 99(5):3111–3116. [PubMed: 11867733]
27. Griswold MA, Jakob PM, Heidemann RM, et al. Generalized autocalibrating partially parallel acquisitions (GRAPPA). Magn Reson Med. 2002; 47(6):1202–1210. [PubMed: 12111967]
28. Gevenois P, De Maertelaer V, De Vuyst P, Zanen J, Yernault JC. Comparison of computed density and macroscopic morphometry in pulmonary emphysema. Am J Respir Crit Care Med. 1995; 152:653–7. [PubMed: 7633722]
29. West B, Matthews L. Stresses, strains, in the lung and surface pressures caused by its weight. J Appl Physiol. 1972; 32(3)
30. Brudin LH, Rhodes CG, Valind SO, Wollmer P, Hughes JM. Regional lung density and blood volume in nonsmoking and smoking subjects measured by PET. J Appl Physiol. 1987; 63(4): 1324–1334. [PubMed: 3500940]
31. Hopkins SR, Henderson AC, Levin DL, et al. Vertical gradients in regional lung density and perfusion in the supine human lung: the Slinky effect. J Appl Physiol. 2007; 103(1):240–248. [PubMed: 17395757]
32. Fichele S, Woodhouse N, Swift AJ, et al. MRI of helium-3 gas in healthy lungs: posture related variations of alveolar size. J Magn Reson Imaging. 2004; 20(2):331–335. [PubMed: 15269962]

33. Evans A, McCormack D, Ouriadov A, Etemad-Rezai R, Santyr G, Parraga G. Anatomical distribution of 3He apparent diffusion coefficients in severe chronic obstructive pulmonary disease. J Magn Reson Imaging. 2007; 26(6):1537–47. [PubMed: 17968961]

34. Snider GL, Kleinerman JL, Thurlbeck WM, Bengally ZH. Definition of emphysema. Report of the National Heart, Lung and Blood Institute, Division of Lung Diseases. Am Rev Respir Dis. 1985; 132:182–185. [PubMed: 4014865]

35. Croxton TL, GGW, SRM, JRH. Future research directions in chronic obstructive pulmonary disease. Am J Respir Crit Care Med. 2002; 165:838–844. [PubMed: 11897653]

36. Vlahovic G, Russell ML, Mercer RR, Crapo JD. Cellular and connective tissue changes in alveolar septal walls in emphysema. Am J Respir Crit Care Med. 1999; 160(6):2086–2092. [PubMed: 10588633]

37. Ruppert, K.; Chang, Y.; Altes, TA., et al. Compartment-selective XTC MRI at 1.5T and 3T. Proceedings of the 17th Scientific Meeting of ISMRM; Honolulu. 2009. (abstract 9)

38. Periaswamy S, Farid H. Elastic registration in the presence of intensity variations. IEEE Trans Med Imaging. 2003; 22(7):865–874. [PubMed: 12906240]

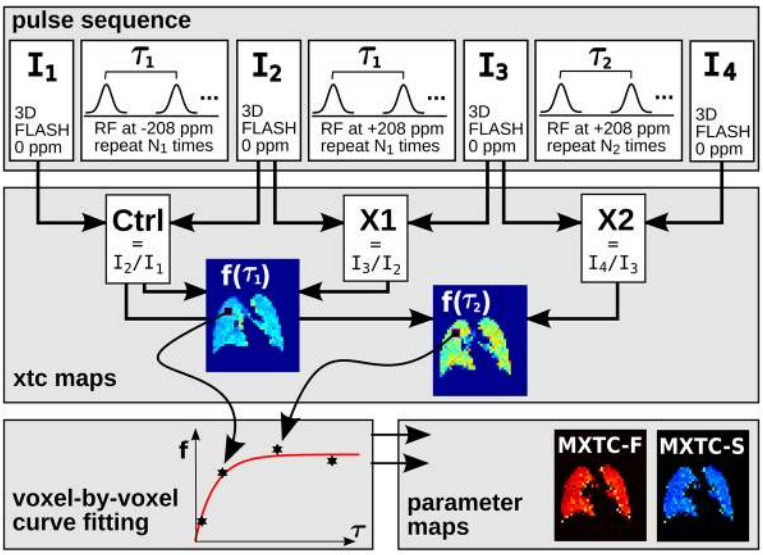

Figure 1.

A schematic showing image-acquisition and data-analysis workflow. Four 3D-FLASH images (I_i) are acquired during a single breath-hold. Between pairs of these 3D-FLASH acquisitions, a series of Gaussian-shaped RF pulses were applied centered either at the dissolved-phase frequency at +208 ppm (XTC contrast, labeled *X1* and *X2*), or at −208 ppm (control contrast, labeled *Ctrl*, for T1 normalization), and separated by a characteristic delay time τ_i. From the image ratios, which were normalized using the data from the control-contrast acquisition and corrected for the different flip angles used in the respective 3D-FLASH acquisitions, depolarization maps ($f(\tau_i)$) were calculated, which reflect the xenon gas-phase magnetization decay due to xenon exchange occurring during a characteristic delay time τ_i. In two to four breath-holds, four to eight depolarization maps were obtained. Curve fitting yielded two parameters for each image voxel: the depolarization value for infinite delay times (MXTC-F) and the square root of the time constant of the xenon exchange (MXTC-S). These fitting parameters are proportional to tissue to alveolar-volume ratio and mean septal wall thickness.

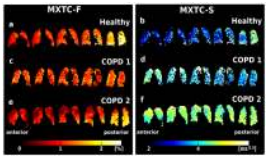

Figure 2.

MXTC parameter maps. The MXTC-F parameter map, which represents regional tissue to alveolar-volume ratio, clearly shows increased parameter values in posterior images for healthy volunteer H1 (a), whereas COPD subject C1 demonstrates no substantial variation in parameter values along the anterior-posterior direction (c), and COPD subject C2 shows regions of decreased parameter values in the upper portions of anterior images (e). The second MXTC parameter, MXTC-S, exhibits increased values in posterior images for the healthy volunteer (b), similar to MXTC-F, whereas the anterior-posterior dependence appears reversed in subject C1 (d). Compared to the healthy volunteer, MXTC-S in subject C2 appears elevated throughout the whole lung (f).

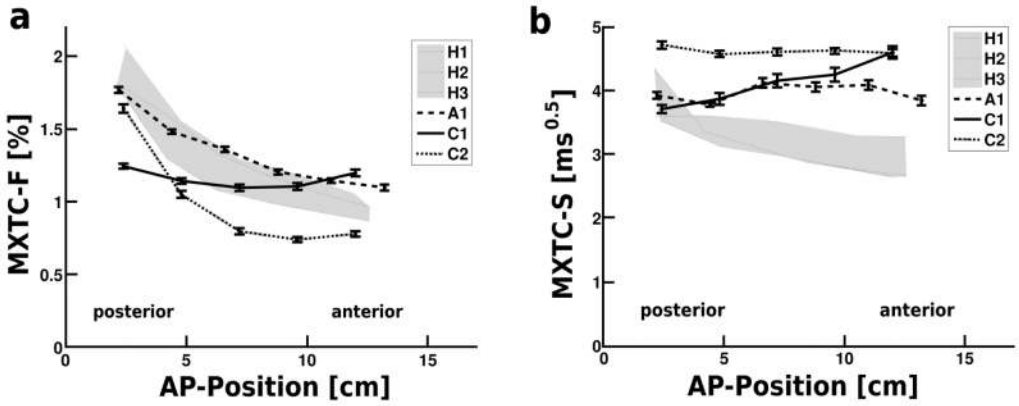

Figure 3.

Dependence of MXTC parameters on lung height. The median values of MXTC-F (a) and MXTC-S (b) for each image are plotted as a function of anterior-posterior (AP) position, measured from the most posterior image. Data from the healthy volunteers (H1–H3) are shown in gray shading, while data from the COPD subjects (C1, C2) and asthmatic subject (A1) are plotted explicitly. Error bars are standard errors of median parameter values. For MXTC-F, the AP-dependence for A1 appears comparable to that for H1–H3, whereas C1 does not show any AP dependence and C2 has lower parameter values in anterior images (a). The MXTC-S parameter appears elevated for the subjects with lung disease (C1, C2, A1), especially in the anterior images, due to the absence of an AP-dependence in comparison to the healthy volunteers (H1–H3) (b).

Figure 4.
Results from CT and HXe129 imaging methods for COPD subject C2. The three imaging techniques depict emphysema in the same regions of the lung, as decreased parameter values in MXTC-F (a) and CT (b) (parameter values with less than −950 HU are colored in red) and increased parameter values in ADC (c).

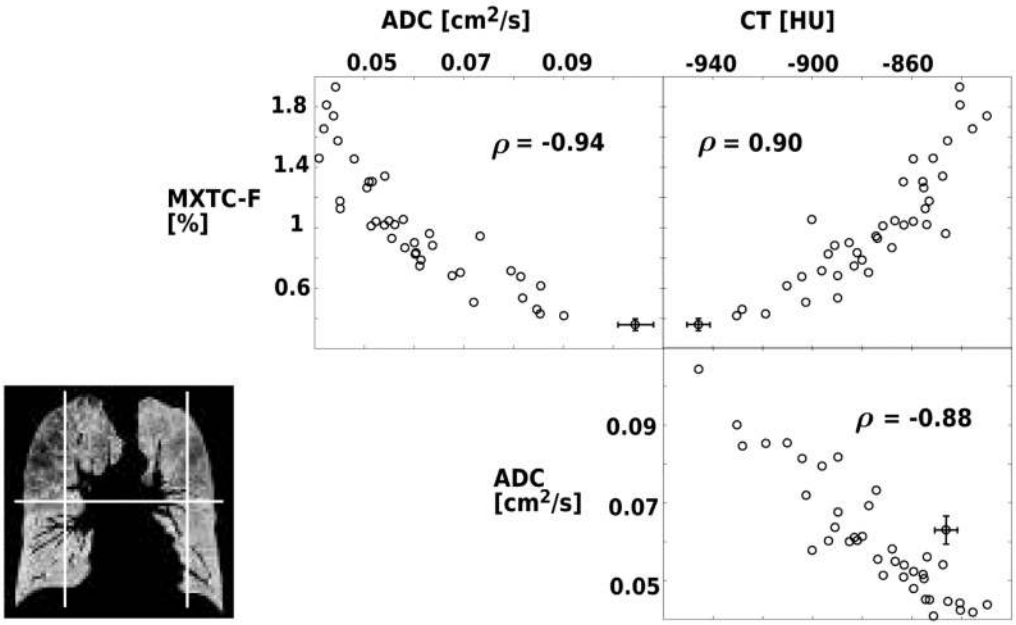

Figure 5.

Regional correlation between HXe129 imaging techniques and CT. ROIs are obtained by dividing each coronal image as shown. Median parameter values for respective ROIs are compared for all techniques. Based on Spearman's ρ value, excellent correlation was found in all cases. Representative error bars correspond to the mean of standard errors of all ROIs.

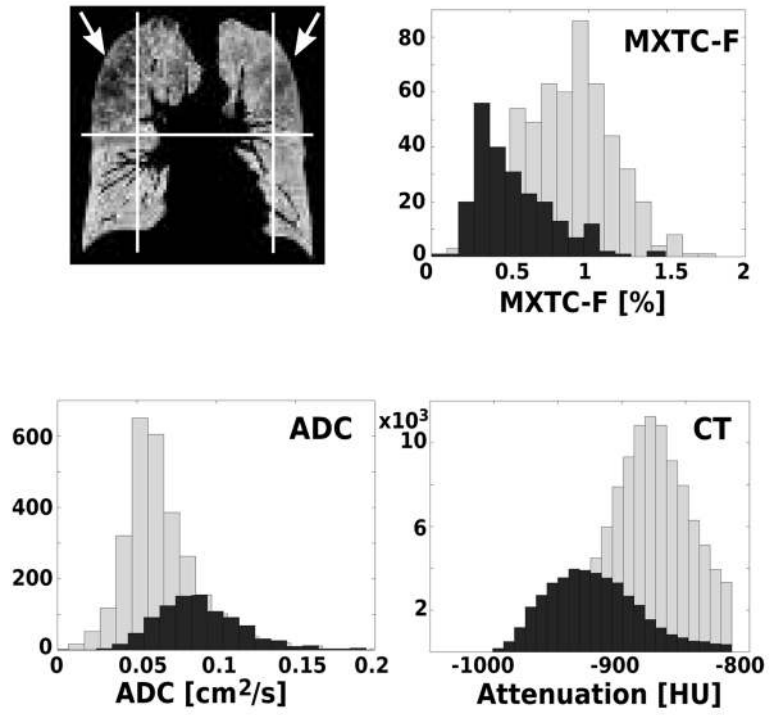

Figure 6.
Comparison of parameter distributions in "emphysematous" (dark bars in plots) and "healthy" (light bars in plots) ROIs for the imaging methods. "Emphysematous" ROIs were defined in anterior partitions as indicated by white arrows.

Table 1

Patient information and summary of imaging results for different modalities

Multiple exchange time Xenon polarization Transfer Contrast (MXTC), Apparent Diffusion Coefficient (ADC) and Computed Tomography (CT). Median (Med) and standard deviation (Std) refer to whole-lung parameter distributions; AP-slope is the slope of linear regression of image median parameter values as a function of image number (to assess the anterior-posterior (AP) parameter dependence); the slope is normalized to the median value (note that this is in negative [HU] units for the CT data) and reported as a percentage change per cm; p-value states the significance of the AP-slope

		H1	H2	H3	C1	C2	A1
Patient Data	**Age [y]**	20	21	19	54	42	48
	Gender	M	M	F	F	F	F
	Health Status	Healthy	Healthy	Healthy	COPD	COPD	Asthma
	FEV1 [% pred]	105	89	104	81	71	74
	FEV1/FVC	0.88	0.83	0.84	0.66	0.66	0.64
MXTC-F	**Med (Std) [%]**	1.1(0.5)	1.4(0.4)	1.4(0.5)	1.2(0.3)	0.9(0.5)	1.3(0.3)
	AP-slope [%]/cm	−7.0	−5.9	−7.0	0.1	−9.1	−4.4
	p-value	0.015	0.001	0.017	0.940	0.067	0.003
MXTC-S	**Med (Std) [$ms^{0.5}$]**	3.2(1.6)	3.5(0.9)	3.1(1.0)	4.1(1.6)	4.6(0.9)	3.9(1.0)
	AP-slope [%]/cm	−4.5	−1.0	−2.8	1.7	−0.2	0.2
	p-value	0.015	0.003	0.004	0.006	0.301	0.743
ADC	**Med (Std)*1e2[cm^2/s]**			3.8(1.5)	5.0(1.9)	6.0(2.9)	
	AP-slope [%]/cm			−0.4	0	3.1	
	p-value			0.524	0.963	0.055	
CT	**Med (Std) [HU]**					−872(40)	
	AP-slope [%]/cm					0.6	
	p-value					0.007	

Table 2

MXTC contrast parameter settings

BH indicates the breath-hold number. $\tau_{1(2)}$ refers to the delay time between contrast-generating RF pulses and $N_{1(2)}$ refers to the number of these pulses during Control contrast and XTC contrast X1 (X2) (see Fig. 1). TA(I) refers to the acquisition time for the gas-phase 3D-FLASH image acquisitions. TA (BH #) gives the total acquisition time for the respective breath-hold

BH #	ID	H1	H2	H3	C1	C2	A1
1	τ_1 [ms]	5	60	40	40	5	5
	N_1	333	70	72	99	186	98
	τ_2 [ms]	60	20	5	10	30	60
	N_2	82	83	152	186	92	65
2	τ_1 [ms]	100	5	60	60	5	100
	N_1	39	152	70	65	259	39
	τ_2 [ms]	20	40	20	20	30	20
	N_2	55	72	83	83	128	55
3	τ_1 [ms]	40	30		5	40	
	N_1	124	75		152	111	
	τ_2 [ms]	10	10		10	10	
	N_2	239	109		109	186	
4	τ_1 [ms]	20				20	
	N_1	184				128	
	τ_2 [ms]	100				15	
	N_2	49				157	
	TA(I) [s]	1.7	2.0	1.5	1.8	1.5	2.2
	TA (BH 1) [s]	15.1	18.0	12.4	17.1	10.5	13.5
	TA (BH 2) [s]	15.8	12.4	15.9	16.8	12.3	17.5
	TA (BH 3) [s]	19.2	13.6		10.0	16.6	
	TA (BH 4) [s]	19.2				13.4	